Handling Nanoparticle Content in Nanocomposite Thin Films Deposited by Misty Plasma Processes through Controlled Flash Boiling Atomization

Simon Chouteau, L. Stafford, Agnès Granier, Antoine Goullet, Mireille Richard-Plouet

Handling nanoparticle content in nanocomposite thin films deposited by misty plasma processes through controlled flash boiling atomization

S. Chouteau[1,2], L. Stafford[2], A. Granier[1,*], A. Goullet[1], M. Richard-Plouet[1]

[1]Nantes Université, CNRS, Institut des Matériaux de Nantes Jean Rouxel, IMN, F-44000 Nantes, France

[2]Département de physique, Université de Montréal, 1375 Ave. Thérèse-Lavoie-Roux, Montréal, Québec, H2V 0B3, Canada

**Corresponding author: agnes.granier@cnrs-imn.fr*

ABSTRACT

Misty plasma processes based on colloidal solutions sprayed into low-pressure plasmas have recently shown great potential for multifunctional thin film deposition. In such processes, nanoparticle accumulation in ring-shaped structures remains the main obstacle to the synthesis of high-quality coatings containing abundant, small-scale, and evenly dispersed nanoparticles. These local buildups appear after a colloidal droplet evaporates on a substrate. Accordingly, controlling the droplets' size in the spray is of key importance to ensure a uniform nanoparticle content in the plasma-deposited nanocomposite film. In this work, it is shown that the use of more volatile solvents produces finer droplets on the substrate, thereby improving nanoparticle dispersion in the matrix. A one-dimensional evaporation model is further developed and used to show that, contrary to what one might expect, this result cannot be attributed to faster evaporation during droplet transport in the low-pressure plasma. Instead, so-called "flash" boiling atomization mechanism is discussed to support the experimental findings.

INTRODUCTION

Thin films have received great attention over the years and are overwhelmingly widespread today. Central to this field of research is the notion of functionality: surface coatings aim to modify a substrate's properties in order to suit a specific use. In this context, multifunctional thin films are now under the spotlight, as they provide multiple properties of interest within a single coating[1–3]. Different strategies exist to achieve multifunctionality. One of them consists in creating a multiphase material known as a nanocomposite, which is obtained after inserting nano-scale objects in a solid matrix[4–6]. Nanocomposite thin films are designed to combine the properties of both the matrix and the nano-reinforcement, and/or to make use of the latter's high surface-to-volume ratio to display interface-like properties on a macroscopic scale. Benefiting from a secured position in conventional thin film deposition, low-temperature plasma processes provide a convenient starting point for the development of reliable nanocomposite growth techniques.

For example, so-called "dusty" plasma methods offer great control over film growth through a wide range of parameters such as ion bombardment energy, working pressure or substrate temperature. Most dusty plasma protocols involve simultaneous plasma-enhanced chemical vapor deposition (PECVD) of the matrix and cathode sputtering of the nanoparticles, allowing for a wide range of matrix/nanoparticles pairs and fine control over film properties and nanoparticles quantity[7,8]. Gas aggregation sources have also been used in this class of processes, as an independent supply of monodisperse nanoparticles[9,10]. Incidentally, one of the biggest challenges regarding nanocomposite thin films deposited by dusty plasma processes relates to the nanoparticles' size. Nanoparticle growth in dusty plasmas is not a linear process, which makes their diameter a delicate parameter to control. Moreover, smaller particles are easily trapped in the plasma volume by electrostatic effects, and tend to aggregate to form larger particles[11]. This last point is especially critical as it affects the final size and distribution of nanoparticles in the films. Particle aggregation remains a major obstacle to the synthesis of nanocomposite thin films containing well-distributed small-scale nanoparticles (< 10 nm).

More recently, studies have shown that sprays of particle-laden liquid droplets in PECVD reactors made decent candidates to address this issue[12–15]. Indeed, in these appropriately labeled "misty" plasma experiments, nanoparticle size management is facilitated since the latter can be prepared beforehand in the form of stable colloidal solutions. In misty plasma processes, nanoparticles are protected from the plasma by the liquid solvent during their transport to the

substrate, which ensures that their size is preserved in the film. In the best-case scenario, nearly all the solvent will have evaporated when the droplets reach the substrate, leaving only the nanoparticles on the sample's surface. Continuous deposition of the thin film matrix will then cover the nanoparticles before the next liquid injection. In practice, however, new challenges arise. First, excessively fast evaporation of highly concentrated colloidal droplets can lead to the formation of large nanoparticles agglomerates before they even reach the substrate, which defeats the purpose of using small-scale particles[16]. Secondly, sessile colloidal droplets evaporating on a surface tend to steer nanoparticles to the edges of the droplet, producing ring-like structures of agglomerated nanoparticles[12,17]. This phenomenon, colloquially known as the "coffee ring effect"[18], is detrimental to the nanocomposite nature of the film. Indeed, although the nanoparticles retain their individual size, their spatial distribution in the matrix is not as uniform as desired.

Many reported misty plasma experiments are focused on atmospheric pressure systems, (suited for polymer matrices), using either plasma jets or dielectric barrier discharges as a plasma source[14,15,19]. A more modest number of studies were conducted at low pressure (suited for dense, inorganic matrices) and showed promising results with regard to nanoparticles quantity and distribution, coffee ring effect put aside. Recently, Mitronika et al.[17] obtained nanocomposite coatings with a high volume fraction of fairly well distributed TiO_2 nanoparticles in SiO_2 matrices using a low-pressure misty plasma reactor. The growth process of nanocomposites in said reactor is now relatively well understood: it was recently shown that the plasma is affected by the presence of droplets, which influences film growth by creating alternating matrix- and nanoparticles-rich deposition steps[20]. The large ring-like structures of agglomerated particles observed in these films remain the main impediment to a homogeneous nanoparticle distribution. In the present work, it is shown that the use of a highly volatile solvent limits this phenomenon and improves nanoparticle distribution in the films by creating smaller droplets. Somewhat unexpectedly, fast evaporation of the solvent is ruled out as an explanation for this result, which is attributed instead to a so-called "flash" boiling atomization process during spray formation. It is further shown that the total amount of nanoparticles in the films can simply be adjusted by modifying the injected suspension's nanoparticle concentration.

EXPERIMENTAL METHODS

1. *Misty plasma reactor*

The hybrid reactor used in this work is based on a low-pressure PECVD system and has been described in detail before[17]. A helicon antenna is used to generate a 13.56 MHz radiofrequency inductively coupled plasma in an oxygen-argon gas mixture (95% O_2, 5% Ar). The applied power is 400 W with negligible reflected power. The residual pressure before plasma deposition is in the order of 10^{-3} mTorr, and the working pressure is 3 mTorr with a main gas flow rate of 24 standard cubic centimeter per minute (SCCM). The plasma diffuses from the source region to a 21 L processing chamber where the sample holder is located. A small 0.11 SCCM flow of hexamethyldisiloxane (HMDSO) vapor is injected in the processing chamber as a precursor for the SiO_2 matrix deposition by PECVD.

A commercial liquid dozer from Kemstream is used to inject sprays of lab-made colloidal solutions in the processing chamber through 5 holes of 100 µm in diameter situated at the injector's nozzle. Liquid injection consists of sequences of 1-ms pulses occurring every minute at a frequency of 0.5 Hz. The number of pulses in a sequence is given by the parameter N. For example, N = 10 results in a sequence of 10 pulses (i.e. 20 seconds total) followed by a 40-seconds period without injection before the next cycle.

2. *Colloidal solutions*

A colloidal solution of anatase TiO_2 nanoparticles was first synthesized according to the protocol described by Karpinski et al.[21], in a solvent mixture of propylene carbonate (PC) and propylene glycol (PG) of molar fraction 27:73 respectively. As synthesized, the nanoparticles are monodisperse, with most nanoparticles having a diameter in the 2-6 nm range, as measured by dynamic light scattering[17]. From this initial suspension, very stable over time, three colloidal solutions were obtained and labeled as follows:

(1) The "low volatility" solution was diluted in 25 vol% methanol, exactly as in Mitronika et al.[17].
(2) The "high volatility" solution was diluted in 75 vol% methanol to increase total volatility.

(3) The "concentrated, high volatility" solution was first concentrated by evaporating the PC/PG suspension to a third of its initial volume, and then diluted in 80 vol% methanol.

Table 1 summarizes the three solutions' final features.

Solution	PC (vol%)	PG (vol%)	MeOH (vol%)	[TiO_2-NP] (g.L-1)	Surface tension (mN.m-1)	Dynamic viscosity (mPa.s)
Low-volatility	20	55	25	3	57	5.5
High-volatility	7	18	75	1	44	1.4
Concentrated, high-volatility	11	9	80	3	43	0.9

Table 1 – Solvent volume fraction, TiO_2 nanoparticles concentration, surface tension, and dynamic viscosity of the three injected colloidal solutions.

It was established in a previous work that the nanoparticles retain their size and crystalline structure after the injection process: although coffee rings are formed, the nanoparticles themselves do not seem to aggregate in larger objects[17]. Their TiO_2 stoichiometry is also preserved, as residual solvent molecules attached to the nanoparticles' surface are chemically etched by the oxygen plasma[22].

3. *Sample characterization*

All films were grown on 1×2 cm (100)-oriented Si substrates. Film thickness and TiO_2 content were obtained by spectroscopic ellipsometry using a J.A. Woollam M-2000 ellipsometer. The SiO_2 matrix model was based on a Cauchy law fitted to data obtained from a plasma-deposited SiO_2 layer in the same reactor, while the TiO_2 nanoparticles model was a custom Tauc-Lorentz dispersion law[22]. Nanocomposite coatings were then modeled as a Bruggeman effective medium approximation (BEMA) of both materials, where the volume fraction of TiO_2 and SiO2 was adjusted to fit the experimental data[17].

After each deposition, samples were imaged using an OMAX optical microscope. Ring-like droplet imprints were hand-counted and their diameters were measured using ImageJ on representative micrographs. 300 to 1200 droplets were counted on each sample to ensure statistical significance. Experimental size counts were plotted on histograms whose bin edges were chosen according to Doane's formula[23]. Lognormal distributions provided the best fit to the data in each case, which hints towards a spray-formation mechanism involving random liquid breakup events

rather than the usual deformations caused by friction with gas (the latter universally results in Gamma-distributed sprays[24,25]. This observation is consistent with the high-vacuum conditions, where the ambient gas is not expected to play a significant role whatsoever.

RESULTS AND DISCUSSION

1. *Experimental results*

Figure 1 presents the droplet imprints' size distribution as observed after 60 minutes deposition at N = 10 pulses per minute, for each solution. Optical micrographs of the sample's surface are also shown in the insets. Table 2 provides the associated average radius and standard deviation, as well as the film's thickness and nanoparticles volume fraction as determined by spectroscopic ellipsometry.

The sample deposited using the initial low-volatility solution (Fig. 1a) presents droplets of diameters in the order of tens of micrometers, which is in the range of what was previously reported in a similar experiment[17]. In addition to the outermost coffee ring shape, larger droplets also display up to 3 internal rings as well as a slightly off-centered eye-like spot in the center. This pattern is typical of the so-called stick-slip behavior during droplet evaporation[26–28]. "Stick" periods are analogous to the coffee ring mechanism: the contact line is pinned to the substrate, and particles accumulate at the droplet edges. Since the droplet has a constant radius but a decreasing volume due to evaporation, its radius is getting increasingly far from its equilibrium value, leading to excess free energy. When this excess energy becomes larger than the line pinning energy barrier, a "slip" period ensues: the droplet jumps to a smaller, closer-to-equilibrium radius depending on its current volume. Alternating stick and slip periods produce the typical multi-ring patterns seen in the inset of Fig. 1a. The uniform stain in the center appears when the radius shrinks to values for which the excess energy is never sufficient to cause the droplet to "slip" again.

Using the more diluted, high-volatility solution a significant impact on droplet size is observed, reducing the average measured radius from 18 to 8.5 µm and making the distribution narrower, with more defined single-ring imprints (Fig 1b). At first glance, the decrease in size appears consistent with the high volatility of methanol compared to that of PC and PG. Since the high-volatility solution contains more methanol than the low-volatility solution in proportion, one would reasonably expect high-volatility droplets to evaporate faster during their transport and therefore to be smaller when they reach the substrate. However, it will be shown in the next section that faster evaporation in the plasma phase is most likely not responsible for the smaller size of the droplets. For now, one can simply acknowledge this result as an improvement regarding nanoparticle distribution in the films. In addition to the reduced droplet size, having methanol as

the main solvent rather than PG could come with a potential beneficial side effect. Since methanol is a much smaller molecule than PC or PG, fewer oxygen radicals are needed to oxidize it fully in H_2O, CO, or CO_2 by interaction with O or O_2 in the plasma. Although verifying it quantitavely falls outside the scope of the present study, this could help mitigating the changes in pressure, plasma composition, and deposition rate observed after each liquid injection[20], and prevent contamination of the matrix by solvent residue since fewer oxidation reactions are needed to "clean up" the substrate after each liquid injection.

However, the improvements gained by diluting the solution in methanol come with an obvious drawback in the context of nanoparticles-rich nanocomposites coatings. Since the colloidal solution is diluted, it is less concentrated and fewer nanoparticles are injected in the same volume of liquid. Yet, a suitable nanocomposite thin films deposition process should allow for a wide, controllable range of nanoparticle content. Therefore, the last solution (concentrated, high volatility solution) was prepared to balance out solvent volatility and nanoparticles concentration. The droplet size distribution obtained with this third solution is shown in Fig. 1c. The average radius is still small (~6 µm), but TiO_2 content in the film is now higher. It could be surprising that the volume fraction of TiO_2 is somewhat different compared to the sample deposited with the low-volatility solution (since the amount of nanoparticles injected is supposed to be the same in both cases). However, one should recall that matrix deposition rate is also affected by liquid injection due to the associated increase in pressure following solvent evaporation[20]. Therefore, different solvents affect deposition rate differently, resulting in different nanoparticle *fractions* in the films.

It is interesting to notice that the BEMA model fits the ellipsometric data better in the case of both methanol-dominant solutions (as indicated by the MSE column in Table 2). Indeed, Bruggeman's approximation needs nano-inclusions to be located in an equivalent mean field, which would not be valid for large-scale clusters of nanoparticles. The fact that the BEMA model describes the data better is an indication that the coatings tend towards a "true" nanocomposite thin film configuration with well-separated nanoparticles. Furthermore, even though clear-cut ring-like imprints were still present on the last sample's surface (Fig. 1c, inset), the film had an overall hazy appearance – contrasting with the monochrome background of the other samples' optical micrographs. Since coffee ring formation is known to occur only above a certain droplet size lower limit (whose value is specific to each suspension)[29], this observation suggests that injecting the

concentrated high-volatility solution produces a mist of droplets sufficiently fine that part of the droplets do not produce ring patterns at all.

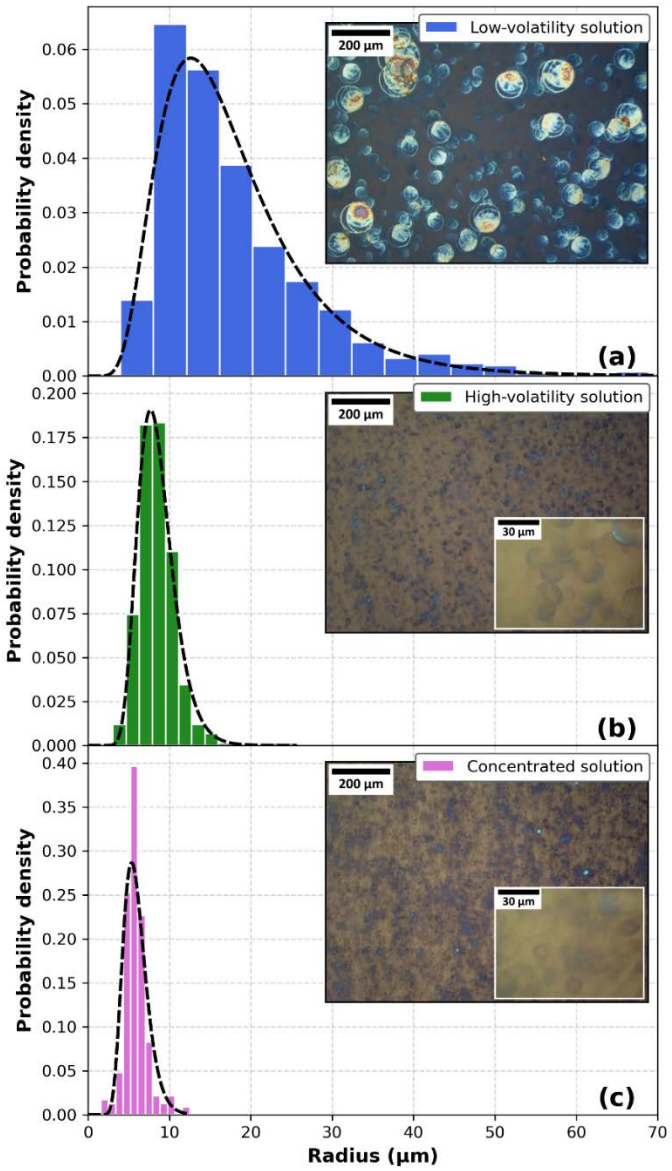

Figure 1 – Droplet imprints size distribution after 60 minutes deposition at N =10 pulses per minute, using the (a) low-volatility (b) high-volatility (c) concentrated high-volatility solution.

Injected solution	Average radius (µm)	Standard deviation (µm)	Film thickness (nm)	TiO_2 in the film (vol%)	MSE
Low-volatility	18	9.9	70.6 ± 3.1	21.6 ± 5.6	103
High-volatility	8.5	2.4	69.2 ± 0.8	7.6 ± 1.2	24
Concentrated, high-volatility	5.9	1.4	59.3 ± 1.3	15.9 ± 2.3	44

Table 2 – Droplet imprints and film properties of nanocomposites deposited at N = 10 pulses for 60 min with three different colloidal solutions, and associated ellipsometry mean standard errors (MSE).

2. Evaporation model

Numerical simulations of the evaporation process during droplet transport were carried out and confronted to the experimental observations. In the model, a single spherical droplet was considered, immersed in an isotropic and stationary plasma. No attempt to account for inter-droplet interaction or nanoparticle influence on the properties of the liquid was made.

For micron-sized droplets evaporating in the mTorr range, the mean free path of evaporating molecules is several orders of magnitude greater than droplet size. Molecules departing from the droplets are therefore in the ballistic, rather than diffusive, regime and re-condensation on the droplet is negligible. For a pure-component droplet, the molar flux Γ_{evap} at its surface can then be evaluated using the Hertz-Knudsen equation:

$$\Gamma_{evap} = \frac{\alpha_e P_{sat}(T_d)}{\sqrt{2\pi M R T_d}} \quad (1)$$

where P_{sat} is the equilibrium vapor pressure of the liquid at temperature T_d, M is the molar mass and R is the universal gas constant. The evaporation coefficient α_e is a dimensionless number between 0 and 1 representing which fraction of the maximum theoretical flux actually evaporates. Contradictory values of α_e are reported in the literature, even for common liquids like water[30], thus we assumed $\alpha_e=1$ for all solvents.

Raoult's law was used to take into account the multi-component nature of the solutions studied here: for an ideal mixture, the partial pressure of each constituent is proportional to its mole fraction in the mixture, leading to the following expression for the total rate of evaporation:

$$\frac{dr_d}{dt} = -\sum_i x_i \Gamma_{evap,i} \frac{M_i}{\rho_i} \quad (2)$$

where r_d is the droplet radius and x_i and ρ_i are the mole fraction and mass density of solvent i, respectively. Consequently, the evolution of the molar content of each constituent in the droplet is:

$$\frac{dN_i}{dt} = -x_i \Gamma_{evap,i} A_d \quad (3)$$

where N_i is the number of moles of solvent i and A_d is the droplet's surface area. Deformations due to momentum, surface charging or any other effect are neglected and A_d is always the surface of a sphere.

The equilibrium vapor pressure term in equation (1) is evaluated using the Clausius-Clapeyron relation:

$$P_{sat} = P_{ref} \exp\left(\frac{H_{vap}}{R_g}\left(\frac{1}{T_{ref}} - \frac{1}{T_d}\right)\right) \quad (4)$$

where P_{ref} is the equilibrium vapor pressure at temperature T_{ref} and H_{vap} is the molar enthalpy of vaporization. The influence of surface tension on vapor pressure (Kelvin effect) is not significant for micrometric or larger droplets and is neglected here. Equation (4) is a function of temperature, the evolution of which with time is obtained from the following energy balance:

$$m_d C_p \frac{dT_d}{dt} = J_{net} A_d \quad (5)$$

where m_d is the droplet's mass, C_p is its specific heat capacity (assumed equal to the weighted-average of the three solvent's respective specific heat capacity), and J_{net} is the total energy flux on the droplet defined as follows:

$$J_{net} = \sigma\left(T_g^4 - T_d^4\right) + \frac{1}{4} n_O v_{th,O} E_{rec,O} - \sum_i x_i \Gamma_{evap,i} \frac{H_{vap,i}}{N_A} \quad (6)$$

where σ is the Stefan-Boltzmann constant, T_g is the gas temperature, n_O is the number density of oxygen atoms in the plasma, $v_{th,O}$ is their thermal velocity, and $E_{rec,O}$ is the energy released by an oxygen-oxygen recombination. The energy balance in equation (6) includes the radiative term, the energy flux due to oxygen recombination at the droplet's surface, and the energy loss associated with every evaporation event. It is assumed that only whole molecules leave the droplet: no evaporation of physically or chemically dissociated fragment is taken into account. The energy fluxes due to collisions with electrons, ions and non-reactive neutrals are negligible here due to the very low density and/or energy of these species in our conditions. The O-O recombination flux was chosen as a reasonable approximation for the heat flux brought to the droplet by the plasma through chemical reactions, which is limited by the flux of O atoms impinging on the droplet's surface. Indeed, even though the oxidation of methanol, PC, and PG release more energy than O-O recombinations, these reactions require several O atoms at the same time in order to be stoichiometric, which leads to similar values for the heat released *per O atom*. In any case, it will be shown in the results that evaporative cooling is the dominant term in our experimental conditions, far ahead the radiative and chemical terms.

The model depicted thus far is based on the assumption that thermal conduction in the liquid is sufficiently fast so that no internal temperature gradient exists in the droplet. This description is known as an isothermal model. However, this assumption may not be valid for the larger droplets observed in our experiments. Therefore, a one-dimensional evaporation model including the internal temperature of the droplets was developed. Only pure liquids are simulated using the one-dimensional model. Spherical symmetry is assumed and the heat equation is solved to obtain the droplet's internal temperature in the radial direction:

$$\rho C_p \frac{\partial T}{\partial t} = \frac{1}{r^2}\frac{\partial}{\partial r}\left(kr^2 \frac{\partial T}{\partial r}\right) \tag{7}$$

where k is the thermal conductivity of the liquid, and r is the radial coordinate. The origin is situated at the droplet's center, where the symmetry condition is applied:

$$\left.\frac{\partial T}{\partial r}\right|_{r=0} = 0 \tag{8}$$

The boundary condition at the droplet's surface follows from the energy balance:

$$-k\left.\frac{\partial T}{\partial r}\right|_{r=r_d} = -J_{net} \tag{9}$$

where J_{net} is calculated using equation (6) for a single liquid (i.e. $x_i=1$). Similarly, equation (2) is used to compute the evaporation rate.

Temperature dependence of the liquids' thermophysical properties was taken into account in both models, based on the available literature. Table 3 summarizes the equations used for the temperature-dependent values of ρ, H_{vap}, C_p, and k, as well as the constant values of P_{ref} and T_{ref}.

Solvent	ρ (kg.m^{-3})	H_{vap} (J.mol^{-1})	C_p (J.kg^{-1}.K^{-1})	k (W.m^{-1}.K^{-1})	P_{ref} (Pa)	T_{ref} (K)	Ref.
Methanol	$1068 - 0.943T$	$40471 - 9.950T$	$684.4 + 6.25T$	$0.225 - 7.29 \times 10^{-5}T$	0.186	178	[31–33]
PC	$1516 - 1.060T$	$77648 - 5.421T$	$916.8 + 2.55T$	$0.194 - 9.98 \times 10^{-5}T$	101325	515	[34–37]
PG	$1258 - 0.757T$	$99745 - 104.1T$	$713.1 - 5.99T$	$0.220 - 7.68 \times 10^{-5}T$	101325	461	[38–41]

Table 3 – Temperature-dependent thermophysical properties of methanol, propylene carbonate, and propylene glycol used in this work.

Equations (7), (8), (9) and the single-component version of equations (2) are solved using an explicit finite difference scheme complying with the Dirichlet criterion: $\frac{(dr)^2}{dt} > \frac{2k}{\rho C_p}$. Each simulation was repeated with different values of *dr* to ensure the results' mesh-independency. In order to compare the two models, the volume-averaged temperature T_{avg} of the droplet in the 1D case was calculated as:

$$T_{avg} = \frac{3}{r_d^3}\int_0^{r_d} T(r) r^2 dr \tag{10}$$

3. *Simulation results*

A 20 ms simulation time was chosen to match the approximate droplet travel time over the range of experimental conditions in the low-pressure reactor, from the direct-liquid-injector to the sample's surface. This travel time was estimated from liquid flow and system geometry: the average volume injected in each 1-ms liquid pulse was measured to be 1.1 µL for all solutions, corresponding to a 1.1 µL/ms liquid flow. Liquid velocity directly at the nozzle exit is then given by $v = q/A_{hyd}$, where q is the liquid flow and A_{hyd} is the total area of the nozzle's opening. With an injector-substrate distance of 40 cm, transport time is about 15 ms and simulations were conducted in this time range. An initial radius of 20 µm was chosen, somewhat arbitrarily, to correspond approximately to the average experimental radius of Fig. 1a.

Figure 2 shows the simulated evaporation of a 20-µm radius droplet for each of the three solutions, using the isothermal model. In the first millisecond, the evaporation rate is strong and the droplets shrink rapidly to a radius of about 19 µm. This small decrease in size is coupled with fast cooling of the droplets due to the endothermic nature of evaporation, after which the latter becomes extremely slow at low temperatures (since vapor pressure is an exponential function of temperature). The results presented here are consistent with the temperatures reported in the literature in both experimental[42–44] and theoretical[12,45] studies. All three solutions display this cooling behavior and the final droplet radius is virtually the same in the three cases, regardless of methanol content. In fact, the vapor pressures of PC and PG are so low that nearly all this initial cooling period is caused solely by the evaporation of methanol, even for the low-volatility solution that only contains 25 vol% of it. This can be better appreciated in Fig. 3, presenting the evolution

of the molar fraction of each solvent during the evaporation of the low-volatility droplet. Figure 3 shows that methanol is sufficiently abundant to cause the rapid cooling phase without entirely disappearing in the 20 ms interval. In other words, since the contribution of PC and PG are almost non-existent, the evaporation dynamics presented in Fig. 2 are essentially those of a methanol droplet; the slight variations being due to the different thermophysical properties of the three solvents. In any case, these variations are too similar to be detected experimentally.

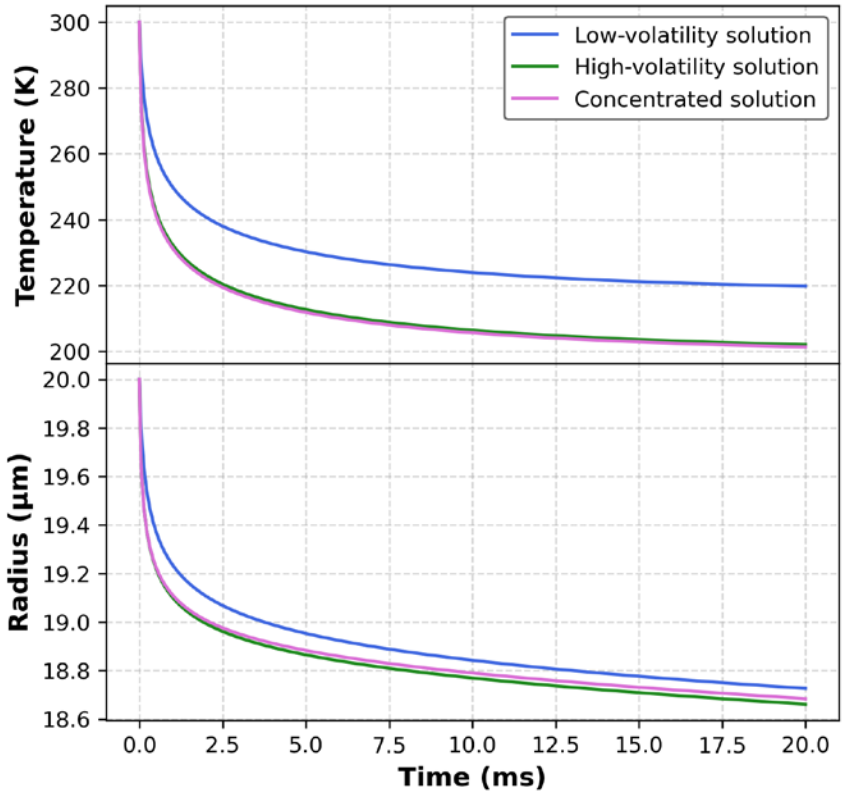

Figure 2 – Evolution of the temperature and radius of 20-µm droplets, according to the isothermal model.

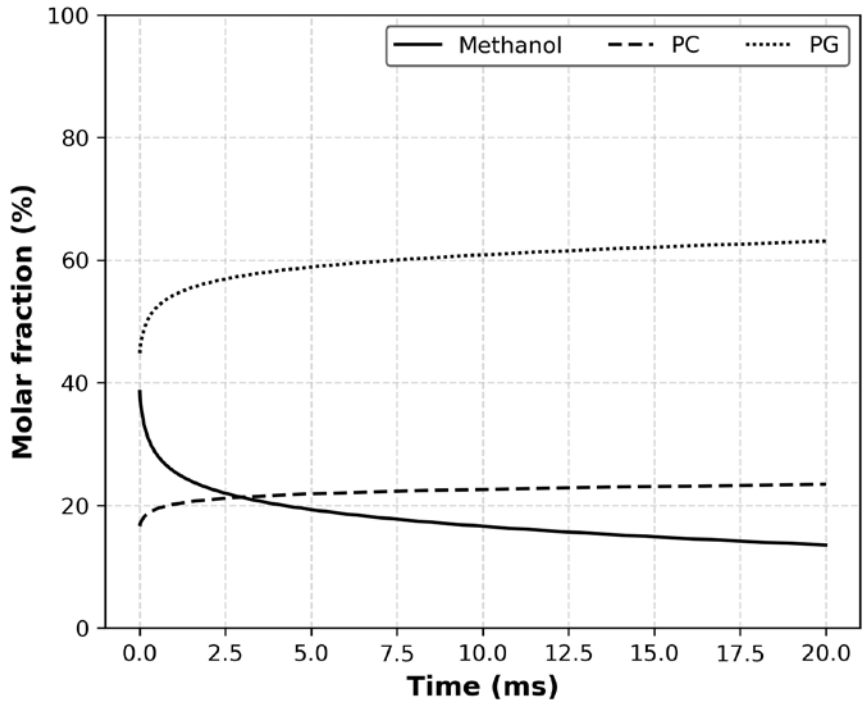

Figure 3 – Evolution of the molar content of an evaporating 20-µm droplets of the low-volatility solution, according to the isothermal model.

It is now clear that the isothermal model does not support the experimental findings of the previous section. However, this discrepancy could be due to an inaccurate description of evaporation by the isothermal model. Indeed, a 20-µm droplet is large enough for an internal temperature gradient to exist. This is illustrated by the Fourier number for heat conduction, which compares the characteristic time scales of heat diffusion with the time interval of interest:

$$Fo = \frac{k\Delta t}{\rho C_p r_d^2} \tag{11}$$

where Fo is the Fourier number and Δt is the time interval of interest. The Fourier number is on the order of unity for a 20-µm radius methanol droplet during a 15-ms interval, which indicates that an internal temperature gradient probably exists during evaporation. In this case, the isothermal model could overestimate the aforementioned initial temperature drop. The isothermal model's validity may then be limited to smaller droplets (or liquids that are more conductive), and the one-dimensional model must be used.

Figure 4 compares the one-dimensional model to the isothermal model for the evaporation of a 20-µm radius methanol droplet. Here the 1D temperature is the volume-averaged temperature,

as defined in equation (10). The two models display globally similar results: the initial temperature drop is less pronounced in the 1D case, which leads to slower evaporation at first. However, the evaporation rate in the 1D case is slightly faster due to a constantly higher temperature. After 20 ms though, the 1D droplet has caught up and its radius is essentially the same as the one calculated with the isothermal description. Although the one-dimensional model was not designed for multi-component liquids and this cannot be rigorously verified yet, it is most likely safe to extrapolate that all solutions will behave in a similar fashion since PC and PG barely contribute to evaporation at all. The divergence between the experimental results of Fig. 1 and the isothermal calculations of Fig. 2 cannot be attributed to an inaccurate description of the internal temperature profile, since the one-dimensional model provides essentially the same results as the isothermal one. Therefore, the results presented in Fig. 2 and 4 strongly suggest that evaporation alone cannot explain why the high-volatility solution produced smaller droplets than the low-volatility solution in the experiments.

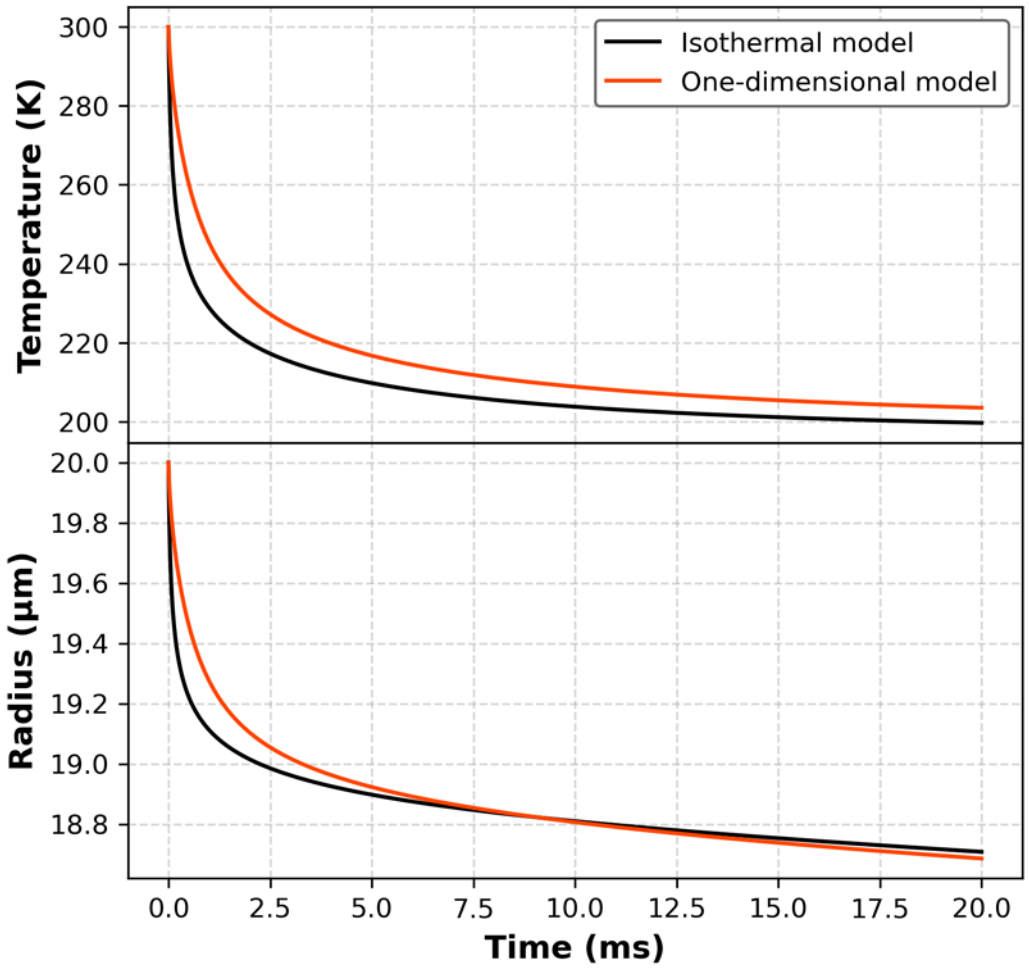

Figure 4 – Evolution of the temperature and radius of a 20-µm methanol droplet, according to the isothermal (black) and one-dimensional (red) models.

4. *Discussion*

Since evaporation from the surface has little to no effect on droplet size during the transport time in the plasma phase, another interpretation of the results presented in Fig. 1 must be formulated. Some of the potential factors can be readily dismissed: first, although surface tension is known to have a limited but measurable influence on droplet size in sprays[24,46], the surface tensions of the three solutions studied in this work (see Table 1) are too similar to cause the shift in size observed in the experimental data. For the same reason, any effect of contact angle on the sample can be ruled out. Electrostatic fragmentation is not expected to affect micron-scale droplets in typical low-pressure plasmas, as described by Coppins[47]. Another suspect would be the solutions' viscosity, which decreases from 5.5 mPa.s for the low-volatility solution to 1.4 mPa.s for the high-volatility solution, as seen in Table 1. Viscosity is known to have a significant effect on droplet size in atmospheric-pressure sprays[48,49]. It is especially important in the Taylor Analogy Breakup (TAB) model, describing the breakup of liquid into droplets as an oscillator damped by viscous forces[50]. However, by definition, viscosity will only be relevant in response to a deformation, which, at atmospheric pressure, is caused by friction with the ambient gas. In the mTorr range, liquid-gas friction is negligible and therefore viscosity is not expected to be as significant.

At such a low pressure however, another breakup phenomenon is more likely to occur. Upon injection, the room-temperature liquid rapidly drops from atmospheric pressure down to a 0.4 Pa vacuum. This isothermal pressure drop is illustrated in Fig. 5, presenting the equilibrium vapor pressures of methanol, PC, and PG as a function of temperature, as calculated using equation (4). Figure 5 shows that, downstream, methanol (and PG, to a lesser extent) reaches a superheated state: the droplet cannot stay liquid at this temperature in the vacuum. Superheating causes what is known as "flash" boiling, where vapor bubbles start to grow in the liquid phase[51,52]. When the volumetric fraction of vapor reaches a critical value (usually on the order of 0.5[53,54]), the liquid bursts into smaller droplets. As depicted in Fig. 6, flash boiling can occur either as flash boiling *atomization*, directly at the output of the injector, or as flash boiling *secondary breakup*, in an already shaped droplet. High superheat degrees ΔT intensify flash boiling processes and lead to improved atomization[54–58].

According to Bushnell and Goodrum's measurements[59], the necessary superheat degree ΔT for flash boiling atomization to occur is fairly well represented by the condition $\Delta T > 0.1T_d$. Out

of the three solvents studied here, only methanol fulfills this requirement unequivocally (see Fig. 5). Therefore, the fraction of methanol in the solutions is indeed a determinant factor of droplet size in the sprays. The greater the amount of methanol (or any high vapor pressure solvent) in the solutions, the further the deviation from equilibrium, and therefore the likelier flash boiling mechanisms appear, thus fostering earlier and more efficient spray atomization. Accordingly, the droplet size reduction seen in the experimental data was indeed directly related to the increased methanol fraction in the solutions, although by flash boiling atomization rather than evaporation.

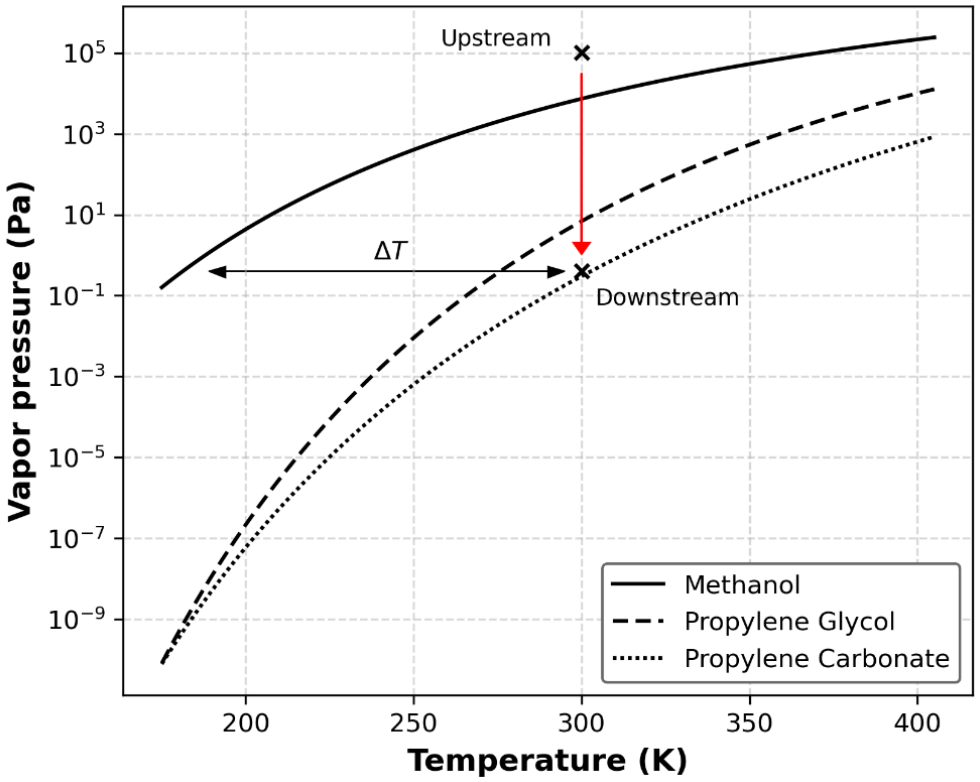

Figure 5 – Calculated vapor pressures of the three liquids versus liquid temperature. The upstream and downstream conditions at the moment of injection are indicated, as well as the high superheat degree ΔT of methanol downstream.

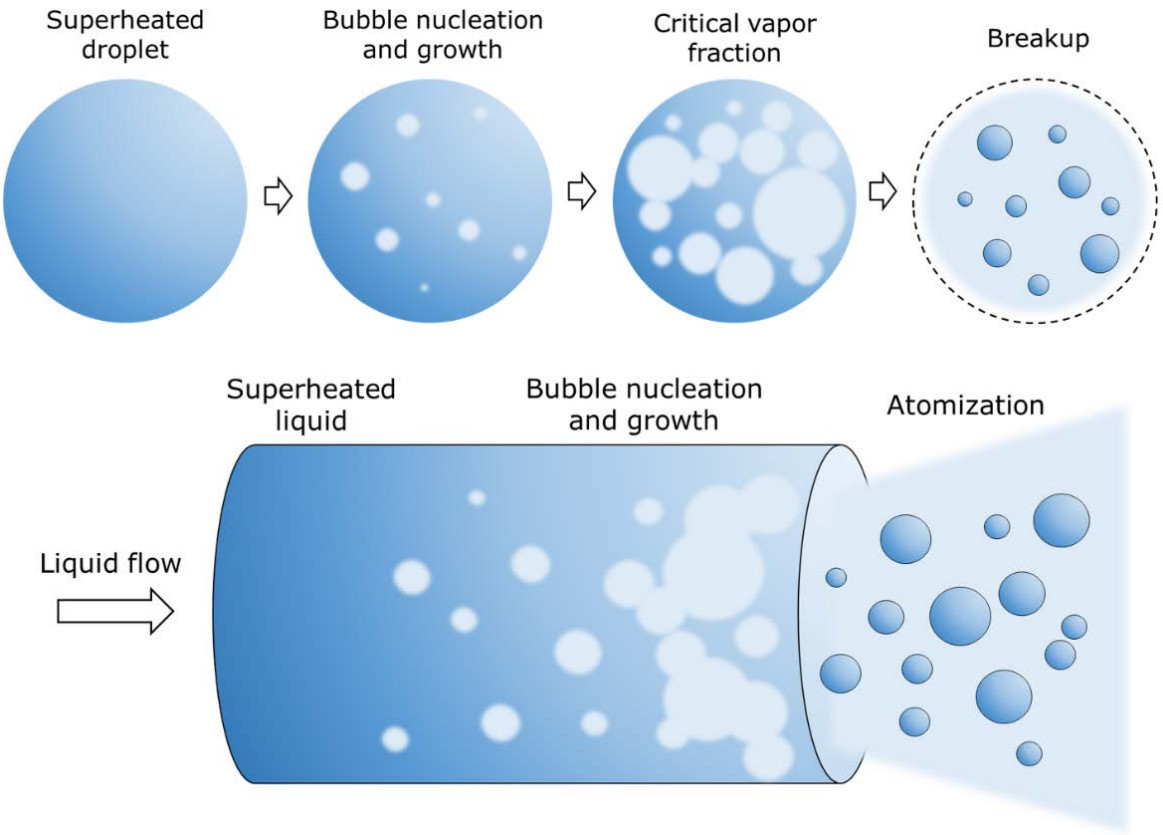

Figure 6 – Diagram of the flash boiling processes. Top: flash boiling secondary breakup. Bottom: flash boiling atomization.

CONCLUSION

In this work, SiO_2/TiO_2 nanocomposite thin films were deposited using a low-pressure misty plasma reactor and three colloidal solutions containing methanol, propylene carbonate and propylene glycol in different proportions. Two main conclusions can be drawn from the experimental results presented above. First, the use of highly volatile solvents will produce smaller droplets and therefore reduce the impact of nanoparticle agglomeration on the nanocomposites' quality. As long as the suspensions stay stable over time, increasing their concentration in nanoparticles provides a direct lever on the nanoparticle fraction in the films. Secondly, over the range of experimental conditions investigated, evaporation from the droplets' surface is barely relevant during transport in the plasma. The critical parameter for the control of droplet size is the deviation from equilibrium at downstream pressure, which is expressed by the superheat degree ΔT. The further from equilibrium, the finer the spray.

ACKNOWLEDGEMENT

The authors gratefully acknowledge the financial support of the CNRS, Université de Montréal and Nantes Université through their contributions to the International Research Network on Controlled Multifunctional Nanomaterials. Mr. Antoine Rovire is thanked for his contribution on the evaporation model.

DATA AVAILABILITY STATEMENT

The data that support the experimental and simulation findings of this study are available upon reasonable request from the authors.

REFERENCES

(1) Faustini, M.; Nicole, L.; Boissière, C.; Innocenzi, P.; Sanchez, C.; Grosso, D. Hydrophobic, Antireflective, Self-Cleaning, and Antifogging Sol−Gel Coatings: An Example of Multifunctional Nanostructured Materials for Photovoltaic Cells. *Chem. Mater.* **2010**, *22* (15), 4406–4413. https://doi.org/10.1021/cm100937e.

(2) Huang, Y.; Zhao, K.; Lu, H.; Jin, K.; He, M.; Chen, Z.; Zhou, Y.; Yang, G. Multifunctional Characteristics of BaNb0.3Ti0.7O3/Si p-n Junctions. *Appl. Phys. Lett.* **2006**, *88* (6), 061919. https://doi.org/10.1063/1.2172290.

(3) *Nanostructures and Thin Films for Multifunctional Applications: Technology, Properties and Devices*; Tiginyanu, I., Topala, P., Ursaki, V., Eds.; NanoScience and Technology; Springer International Publishing: Cham, 2016. https://doi.org/10.1007/978-3-319-30198-3.

(4) Guldin, S.; Kohn, P.; Stefik, M.; Song, J.; Divitini, G.; Ecarla, F.; Ducati, C.; Wiesner, U.; Steiner, U. Self-Cleaning Antireflective Optical Coatings. *Nano Letters* **2013**, *13* (11), 5329–5335. https://doi.org/10.1021/nl402832u.

(5) Jeevanandam, J.; Barhoum, A.; Chan, Y. S.; Dufresne, A.; Danquah, M. K. Review on Nanoparticles and Nanostructured Materials: History, Sources, Toxicity and Regulations. *Beilstein J. Nanotechnol.* **2018**, *9* (1), 1050–1074. https://doi.org/10.3762/bjnano.9.98.

(6) Laiho, A.; Majumdar, H. S.; Baral, J. K.; Jansson, F.; Österbacka, R.; Ikkala, O. Tuning the Electrical Switching of Polymer/Fullerene Nanocomposite Thin Film Devices by Control of Morphology. *Appl. Phys. Lett.* **2008**, *93* (20), 203309. https://doi.org/10.1063/1.3033221.

(7) Despax, B.; Raynaud, P. Deposition of “Polysiloxane” Thin Films Containing Silver Particles by an RF Asymmetrical Discharge. *Plasma Processes and Polymers* **2007**, *4* (2), 127–134. https://doi.org/10.1002/ppap.200600083.

(8) Milella, A.; Palumbo, F.; Dilonardo, E.; Barucca, G.; Cosma, P.; Fracassi, F. Single Step Plasma Deposition of Platinum-Fluorocarbon Nanocomposite Films as Electrocatalysts of Interest for Micro Fuel Cells Technology. *Plasma Processes and Polymers* **2014**, *11* (11), 1068–1075. https://doi.org/10.1002/ppap.201400039.

(9) Hanuš, J.; Steinhartová, T.; Kylián, O.; Kousal, J.; Malinský, P.; Choukourov, A.; Macková, A.; Biederman, H. Deposition of Cu/a-C:H Nanocomposite Films. *Plasma Processes and Polymers* **2016**, *13* (9), 879–887. https://doi.org/10.1002/ppap.201500208.
(10) Košutová, T.; Horák, L.; Shelemin, A.; Vaidulych, M.; Hanuš, J.; Biederman, H.; Kylián, O.; Solař, P.; Cieslar, M.; Choukourov, A.; Dopita, M. Synthesis and Microstructure Investigation of Heterogeneous Metal-Plasma Polymer Ag/HMDSO Nanoparticles. *Surface and Interface Analysis* **2020**, *52* (12), 1023–1028. https://doi.org/10.1002/sia.6779.
(11) Melzer, A. *Physics of Dusty Plasmas: An Introduction*; Lecture Notes in Physics; Springer International Publishing: Cham, 2019; Vol. 962. https://doi.org/10.1007/978-3-030-20260-6.
(12) Ogawa, D.; Saraf, I.; Sra, A.; Timmons, R.; Goeckner, M.; Overzet, L. The Direct Injection of Liquid Droplets into Low Pressure Plasmas. *Journal of Vacuum Science & Technology A: Vacuum, Surfaces, and Films* **2009**, *27* (2), 342–351. https://doi.org/10.1116/1.3081965.
(13) Ross, A. D.; Gleason, K. K. The CVD of Nanocomposites Fabricated via Ultrasonic Atomization. *Chemical Vapor Deposition* **2006**, *12* (4), 225–230. https://doi.org/10.1002/cvde.200506368.
(14) Dembele, A.; Rahman, M.; Reid, I.; Twomey, B.; MacElroy, J. M. D.; Dowling, D. P. Deposition of Hybrid Organic–Inorganic Composite Coatings Using an Atmospheric Plasma Jet System. *Journal of Nanoscience and Nanotechnology* **2011**, *11* (10), 8730–8737. https://doi.org/10.1166/jnn.2011.3459.
(15) Liguori, A.; Traldi, E.; Toccaceli, E.; Laurita, R.; Pollicino, A.; Focarete, M. L.; Colombo, V.; Gherardi, M. Co-Deposition of Plasma-Polymerized Polyacrylic Acid and Silver Nanoparticles for the Production of Nanocomposite Coatings Using a Non-Equilibrium Atmospheric Pressure Plasma Jet. *Plasma Processes and Polymers* **2016**, *13* (6), 623–632. https://doi.org/10.1002/ppap.201500143.
(16) Profili, J.; Levasseur, O.; Blaisot, J.-B.; Koronai, A.; Stafford, L.; Gherardi, N. Nebulization of Nanocolloidal Suspensions for the Growth of Nanocomposite Coatings in Dielectric Barrier Discharges: Nebulization of Nanocolloidal Suspensions…. *Plasma Processes and Polymers* **2016**, *13* (10), 981–989. https://doi.org/10.1002/ppap.201500223.
(17) Mitronika, M.; Profili, J.; Goullet, A.; Gautier, N.; Stephant, N.; Stafford, L.; Granier, A.; Richard-Plouet, M. TiO2–SiO2 Nanocomposite Thin Films Deposited by Direct Liquid Injection of Colloidal Solution in an O2/HMDSO Low-Pressure Plasma. *J. Phys. D: Appl. Phys.* **2021**, *54* (8), 085206. https://doi.org/10.1088/1361-6463/abc84d.
(18) Deegan, R. D.; Bakajin, O.; Dupont, T. F.; Huber, G.; Nagel, S. R.; Witten, T. A. Capillary Flow as the Cause of Ring Stains from Dried Liquid Drops. *Nature* **1997**, *389* (6653), 827–829. https://doi.org/10.1038/39827.
(19) Fanelli, F.; Mastrangelo, A. M.; Fracassi, F. Aerosol-Assisted Atmospheric Cold Plasma Deposition and Characterization of Superhydrophobic Organic–Inorganic Nanocomposite Thin Films. *Langmuir* **2014**, *30* (3), 857–865. https://doi.org/10.1021/la404755n.
(20) Chouteau, S.; Mitronika, M.; Goullet, A.; Richard-Plouet, M.; Stafford, L.; Granier, A. Kinetics Driving Nanocomposite Thin-Film Deposition in Low-Pressure Misty Plasma Processes. *J. Phys. D: Appl. Phys.* **2022**, *55* (50), 505303. https://doi.org/10.1088/1361-6463/ac9ac2.
(21) Karpinski, A.; Berson, S.; Terrisse, H.; Mancini-Le Granvalet, M.; Guillerez, S.; Brohan, L.; Richard-Plouet, M. Anatase Colloidal Solutions Suitable for Inkjet Printing: Enhancing Lifetime of Hybrid Organic Solar Cells. *Solar Energy Materials and Solar Cells* **2013**, *116*, 27–33. https://doi.org/10.1016/j.solmat.2013.04.006.

(22) Mitronika, M.; Profili, J.; Goullet, A.; Stafford, L.; Granier, A.; Richard-Plouet, M. Modification of the Optical Properties and Nano-Crystallinity of Anatase TiO2nanoparticles Thin Film Using Low Pressure O2 Plasma Treatment. *Thin Solid Films* **2020**, *709*, 138212. https://doi.org/10.1016/j.tsf.2020.138212.
(23) Doane, D. P. Aesthetic Frequency Classifications. *The American Statistician* **1976**, *30* (4), 181–183. https://doi.org/10.1080/00031305.1976.10479172.
(24) Kooij, S.; Sijs, R.; Denn, M. M.; Villermaux, E.; Bonn, D. What Determines the Drop Size in Sprays? *Physical Review X* **2018**, *8* (3). https://doi.org/10.1103/PhysRevX.8.031019.
(25) Villermaux, E. Fragmentation. *Annual Review of Fluid Mechanics* **2007**, *39* (1), 419–446. https://doi.org/10.1146/annurev.fluid.39.050905.110214.
(26) Shanahan, M. E. R. Simple Theory of "Stick-Slip" Wetting Hysteresis. *Langmuir* **1995**, *11* (3), 1041–1043. https://doi.org/10.1021/la00003a057.
(27) Moffat, J. R.; Sefiane, K.; Shanahan, M. E. R. Effect of TiO2 Nanoparticles on Contact Line Stick−Slip Behavior of Volatile Drops. *J. Phys. Chem. B* **2009**, *113* (26), 8860–8866. https://doi.org/10.1021/jp902062z.
(28) Wu, M.; Man, X.; Doi, M. Multi-Ring Deposition Pattern of Drying Droplets. *Langmuir* **2018**, *34* (32), 9572–9578. https://doi.org/10.1021/acs.langmuir.8b01655.
(29) Shen, X.; Ho, C.-M.; Wong, T.-S. Minimal Size of Coffee Ring Structure. *J. Phys. Chem. B* **2010**, *114* (16), 5269–5274. https://doi.org/10.1021/jp912190v.
(30) Persad, A. H.; Ward, C. A. Expressions for the Evaporation and Condensation Coefficients in the Hertz-Knudsen Relation. *Chem. Rev.* **2016**, *116* (14), 7727–7767. https://doi.org/10.1021/acs.chemrev.5b00511.
(31) Waliszewski, D. Heat Capacities of the Mixtures of Ionic Liquids with Methanol at Temperatures from 283.15K to 323.15K. *The Journal of Chemical Thermodynamics* **2008**, *40* (2), 203–207. https://doi.org/10.1016/j.jct.2007.07.001.
(32) Coquelet, C.; Valtz, A.; Richon, D.; de la Fuente, J. C. Volumetric Properties of the Boldine+alcohol Mixtures at Atmospheric Pressure from 283.15 to 333.15K: A New Method for the Determination of the Density of Pure Boldine. *Fluid Phase Equilibria* **2007**, *259* (1), 33–38. https://doi.org/10.1016/j.fluid.2007.04.030.
(33) Vercher, E.; González-Alfaro, V.; Llopis, F. J.; Orchillés, A. V.; Miguel, P. J.; Martínez-Andreu, A. Thermophysical Properties of Binary Mixtures of 1-Butyl-1-Methylpyrrolidinium Trifluoromethanesulfonate Ionic Liquid with Alcohols at Several Temperatures. *The Journal of Chemical Thermodynamics* **2018**, *118*, 292–301. https://doi.org/10.1016/j.jct.2017.12.009.
(34) Verevkin, S. P.; Toktonov, A. V.; Chernyak, Y.; Schäffner, B.; Börner, A. Vapour Pressure and Enthalpy of Vaporization of Cyclic Alkylene Carbonates. *Fluid Phase Equilibria* **2008**, *268* (1–2), 1–6. https://doi.org/10.1016/j.fluid.2008.03.013.
(35) Harris, K. R.; Kanakubo, M. Self-Diffusion Coefficients and Related Transport Properties for a Number of Fragile Ionic Liquids. *J. Chem. Eng. Data* **2016**, *61* (7), 2399–2411. https://doi.org/10.1021/acs.jced.6b00021.
(36) Pires, J.; Timperman, L.; Jacquemin, J.; Balducci, A.; Anouti, M. Density, Conductivity, Viscosity, and Excess Properties of (Pyrrolidinium Nitrate-Based Protic Ionic Liquid+propylene Carbonate) Binary Mixture. *The Journal of Chemical Thermodynamics* **2013**, *59*, 10–19. https://doi.org/10.1016/j.jct.2012.11.020.
(37) Tuliszka, M.; Jaroszyk, F.; Portalski, M. Absolute Measurement of the Thermal Conductivity of Propylene Carbonate by the AC Transient Hot-Wire Technique. *Int J Thermophys* **1991**, *12* (5), 791–800. https://doi.org/10.1007/BF00502406.

(38) Steele, W. V.; Chirico, R. D.; Knipmeyer, S. E.; Nguyen, A. Measurements of Vapor Pressure, Heat Capacity, and Density along the Saturation Line for ε-Caprolactam, Pyrazine, 1,2-Propanediol, Triethylene Glycol, Phenyl Acetylene, and Diphenyl Acetylene. *J. Chem. Eng. Data* **2002**, *47* (4), 689–699. https://doi.org/10.1021/je010085z.
(39) Sun, T.; Teja, A. S. Density, Viscosity and Thermal Conductivity of Aqueous Solutions of Propylene Glycol, Dipropylene Glycol, and Tripropylene Glycol between 290 K and 460 K. *J. Chem. Eng. Data* **2004**, *49* (5), 1311–1317. https://doi.org/10.1021/je049960h.
(40) Sagdeev, D.; Fomina, M.; Alyaev, V.; Musin, R.; Abdulagatov, I. Density of Working Liquids for Diffusion Vacuum Pumps. *J. Chem. Eng. Data* **2018**, *63* (5), 1698–1705. https://doi.org/10.1021/acs.jced.8b00028.
(41) Li, C.-K.; Soriano, A. N.; Li, M.-H. Heat Capacities of the Mixed-Solvents Desiccants (Glycols+water+salts). *Thermochimica Acta* **2009**, *487* (1), 26–32. https://doi.org/10.1016/j.tca.2009.01.008.
(42) Wilson, K. R.; Rude, B. S.; Smith, J.; Cappa, C.; Co, D. T.; Schaller, R. D.; Larsson, M.; Catalano, T.; Saykally, R. J. Investigation of Volatile Liquid Surfaces by Synchrotron X-Ray Spectroscopy of Liquid Microjets. *Review of Scientific Instruments* **2004**, *75* (3), 725–736. https://doi.org/10.1063/1.1645656.
(43) Goy, C.; Potenza, M. A. C.; Dedera, S.; Tomut, M.; Guillerm, E.; Kalinin, A.; Voss, K.-O.; Schottelius, A.; Petridis, N.; Prosvetov, A.; Tejeda, G.; Fernández, J. M.; Trautmann, C.; Caupin, F.; Glasmacher, U.; Grisenti, R. E. Shrinking of Rapidly Evaporating Water Microdroplets Reveals Their Extreme Supercooling. *Phys. Rev. Lett.* **2018**, *120* (1), 015501. https://doi.org/10.1103/PhysRevLett.120.015501.
(44) Drisdell, W. S.; Cappa, C. D.; Smith, J. D.; Saykally, R. J.; Cohen, R. C. Determination of the Evaporation Coefficient of D₂O. *Atmos. Chem. Phys.* **2008**, *8* (22), 6699–6706. https://doi.org/10.5194/acp-8-6699-2008.
(45) Kazemi, M. A.; Zandavi, S. H.; Zargartalebi, M.; Sinton, D.; Elliott, J. A. W. Analysis of the Evaporation Coefficients of Water, Heavy Water, and Methanol in a High Vacuum Environment. *International Journal of Heat and Mass Transfer* **2023**, *204*, 123833. https://doi.org/10.1016/j.ijheatmasstransfer.2022.123833.
(46) Sijs, R.; Kooij, S.; Bonn, D. How Surfactants Influence the Drop Size in Sprays from Flat Fan and Hollow Cone Nozzles. *Physics of Fluids* **2021**, *33* (11), 113608. https://doi.org/10.1063/5.0066775.
(47) Coppins, M. Electrostatic Breakup in a Misty Plasma. *Phys. Rev. Lett.* **2010**, *104* (6), 065003. https://doi.org/10.1103/PhysRevLett.104.065003.
(48) Dayal, P.; Shaik, M. S.; Singh, M. Evaluation of Different Parameters That Affect Droplet-size Distribution from Nasal Sprays Using the Malvern Spraytec®. *Journal of Pharmaceutical Sciences* **2004**, *93* (7), 1725–1742. https://doi.org/10.1002/jps.20090.
(49) Ishak, M. H. H.; Ismail, F.; Mat, S. C.; Aziz, M. S. A.; Abdullah, M. Z.; Abas, A. Numerical Study on the Influence of Nozzle Spray Shape on Spray Characteristics Using Diesel and Biofuel Blends. *Biofuels* **2021**, *12* (9), 1109–1121. https://doi.org/10.1080/17597269.2019.1583717.
(50) O'Rourke, P. J.; Amsden, A. A. The Tab Method for Numerical Calculation of Spray Droplet Breakup; 1987; p 872089. https://doi.org/10.4271/872089.
(51) Sher, E.; Bar-Kohany, T.; Rashkovan, A. Flash-Boiling Atomization. *Progress in Energy and Combustion Science* **2008**, *34* (4), 417–439. https://doi.org/10.1016/j.pecs.2007.05.001.
(52) Bhatia, B.; De, A. Flash Boiling in Sprays: Recent Developments and Modeling. *J Indian Inst Sci* **2019**, *99* (1), 93–104. https://doi.org/10.1007/s41745-019-0104-x.

(53) Kawano, D.; Goto, Y.; Odaka, M.; Senda, J. Modeling Atomization and Vaporization Processes of Flash-Boiling Spray; 2004; pp 2004-01–0534. https://doi.org/10.4271/2004-01-0534.
(54) Zeng, Y.; Lee, C.-F. F. An Atomization Model for Flash Boiling Sprays. *Combustion Science and Technology* **2001**, *169* (1), 45–67. https://doi.org/10.1080/00102200108907839.
(55) Chen, Q.; M, K. Ja.; Li, Y.; Chua, K. J. Experimental and Mathematical Study of the Spray Flash Evaporation Phenomena. *Applied Thermal Engineering* **2018**, *130*, 598–610. https://doi.org/10.1016/j.applthermaleng.2017.11.018.
(56) Wang, J.-X.; Guo, W.; Xiong, K.; Wang, S.-N. Review of Aerospace-Oriented Spray Cooling Technology. *Progress in Aerospace Sciences* **2020**, *116*, 100635. https://doi.org/10.1016/j.paerosci.2020.100635.
(57) Zeng, W.; Xu, M.; Zhang, G.; Zhang, Y.; Cleary, D. J. Atomization and Vaporization for Flash-Boiling Multi-Hole Sprays with Alcohol Fuels. *Fuel* **2012**, *95*, 287–297. https://doi.org/10.1016/j.fuel.2011.08.048.
(58) Xi, X.; Liu, H.; Jia, M.; Xie, M.; Yin, H. A New Flash Boiling Model for Single Droplet. *International Journal of Heat and Mass Transfer* **2017**, *107*, 1129–1137. https://doi.org/10.1016/j.ijheatmasstransfer.2016.11.027.
(59) Bushnell, D. M.; Gooderum, P. B. Atomization of Superheated Water Jets at Low Ambient Pressures. *Journal of Spacecraft and Rockets* **1968**, *5* (2), 231–232. https://doi.org/10.2514/3.29227.

TABLE OF CONTENTS GRAPHIC